SUPPORTING INFORMATION

Hybrid Electrolytes with Ultrahigh Li-Ion Transference Number for Lithium-Metal Batteries with Fast and Stable Charge/Discharge Capability

Xiaoyan Zhou,[a] Xiaogang Li,[b] Zhuo Li,[a] Huixin Xie,[a] Jialong Fu [a] Lu Wei,[a] Hui Yang,[b] Xin Guo[a]**

[a] *State Key Laboratory of Material Processing and Die & Mould Technology, Laboratory of Solid State Ionics, School of Materials Science and Engineering, Huazhong University of Science and Technology, Wuhan 430074, P.R. China*

[b] *Department of Mechanics, School of Aerospace Engineering, Huazhong University of Science and Technology, Wuhan 430074, P.R. China*

E-mails: *xguo@hust.edu.cn (X.G.); huiyang2017@hust.edu.cn (H.Y.)*

Experimental Section

1. Materials preparation. α-$LiAlO_2$@γ-Al_2O_3 (LAO) nanosheets were prepared by a simple solvothermal method and a subsequent annealing treatment. The precursor was firstly prepared by mixing 0.5 g sodium dodecyl sulfate (SDS, AR, Aladdin), 5 mmol urea (AR, Sinopharm), 5 mmol aluminium iso-propoxide (AR, Aladdin), and 50 mL mixed solution of absolute ethanol (AR, Sinopharm)/ethylene glycol (AR, Sinopharm) (4:1 by *v:v*) under vigorous stirring for 3 h. Then the precursor was transferred into a 100 mL Teflon-lined autoclave and heated at 110 °C for 12 h. The obtained products were centrifuged and washed with ethanol and distilled water for several times, and then dried at 75 °C overnight. Afterwards, 3 g obtained white powder was collected and mixed with 0.3 g lithium carbonate (AR, Sinopharm) in absolute ethanol and dried at 60 °C. Finally, the collected white powder was calcined at 700 °C for 3 h to obtain the final LAO nanosheets.

2. Preparation of LAO-PVDF electrolytes. PVDF-HFP (M_w = 400 000, Aladdin) and LAO nanosheets were dried in vacuum at 60 °C for 12 h before use. 0.3 g PVDF-HFP was dissolved in a mixed solvent of 3 mL anhydrous acetone (AR, Sinopharm) and 2 mL absolute ethanol under magnetic stirring at 60 °C for 2 h, then different amounts of LAO nanosheets (2 wt.%, 5 wt.%, 10 wt.%, 15 wt.%) were added and stirred for another 3 h to get homogeneous slurries. To produce flexible composite electrolyte membranes, the slurries were casted on slide and dried for 4 h at room temperature, and then kept at 60 ℃ overnight in vacuum. Subsequently, the as-prepared *x*% LAO-PVDF membranes were cut into circular shape with a diameter of 16 mm, and immersed in liquid electrolyte (1 M $LiPF_6$/EC:DMC:EMC(1:1:1 by *v:v:v*)/1% VC) for 12 h for activation, finally *x*% LAO-PVDF (*x* = 2, 5, 10, 15) electrolytes were obtained.

3. Structural and property characterizations. Crystal structures of samples were

examined by a Shinadu X-ray diffractometer (XRD) with nickel-filtered Cu Kα radiation (k = 1.5418 Å) over the 2θ range of 10 to 80°. The morphologies of various samples were investigated by scanning electron microscope (SEM, Zeiss SUPRA55), environmental scanning electron microscope (ESEM, Quanta 200), and transmission electron microscope (TEM, JEOL JEM−2100F). Nitrogen adsorption/desorption curves were obtained by a Micrometrics ASAP 2020 plus at 77 K, the specific surface areas were calculated according to the Brunauer–Emmett–Teller (BET) equation, and the pore size distribution was determined based on the nitrogen gas adsorption isotherm. Diamond DSC and Pyris 1 TGA were performed to acquire the phase transition temperature and evaluate the electrolyte thermal stability using a heating rate of 10 ^{o}C min^{-1} in nitrogen. The mechanical strength of the LAO-PVDF membranes were measured with Instron Tensile Teser at a loading rate of 5 mm/min at room temperature. X-ray photoelectron spectroscopy (XPS) investigations were performed on an AXIS-ULTRA DLD-600W spectrometer, the XPS spectra were calibrated by C *1s* peak at 284.6 eV and then fitted based on Gaussian-Lorentzian functions. Raman spectra (Lab RAM HR800) and FTIR (VERTEX 70) were obtained at the ambient temperature to investigate the interactions between LAO and LEs.

The electrolyte uptakes and retentions of different types of hybrid polymer electrolytes were measured as follows: completely dried LAO-PVDF membrane was weighed, and then immersed in liquid electrolytes for 12 h. Extra electrolyte on the membrane surface was rubbed away and weighed again. The value of electrolyte uptake was then calculated from [1, 2] :

$$Electrolyte\ Uptake = \frac{W_b - W_a}{W_a} \times 100\% \quad \text{(S1)}$$

where W_a and W_b are the weights of the LAO-PVDF membrane before and after

immersing in the liquid electrolyte for 2 h, respectively. Afterwards, the LAO-PVDF membrane was kept in the air for 10, 20, 30, 50, 70, 100, 120, 160, 230 min and weighed again. The electrolyte retention value was then calculated according to:

$$Electrolyte\ Retention = \frac{W_t - W_b}{W_b} \times 100\% \tag{S2}$$

where W_t is the electrolyte weights after 10, 20, 30, 50, 70, 100, 120, 160 and 230 min.

4. Electrochemical measurements. Ionic conductivities of the electrolytes were measured on symmetric cells with two stainless steel electrodes by an electrochemical workstation (Solarton 1260 impedance analyzer) with an alternating-current (AC) amplitude of 5 mV over the frequency range from 1 MHz to 1 Hz and a temperature range from –30 to 60 °C. The sample was heated at desired temperatures for half an hour before each measurement. The bulk resistance of the electrolyte membrane (R) was determined by the intercept of the Nyquist plot with the real axis. The ionic conductivity was calculated from:

$$\sigma = \frac{d}{R \times S} \tag{S3}$$

where d is the thickness and S is the contact area of the electrolyte and the electrode. By measuring and fitting the ionic conductivity as a function of temperature (T), the activation energy (E_a) could be derived from the Vogel-Tammann-Fulcher (VTF) equation:

$$\sigma = AT^{-1/2} \exp\left(\frac{-E_a}{R(T - T_0)}\right) \tag{S4}$$

where A is the pre-exponential factor, R is the ideal gas constant, and T_0 is the Vogel scaling temperature related to the glass transition temperature (T_g), at which the free volume disappears.

The electrochemical stability window of the electrolyte was measured through LSV at a scan rate of 10 mV s^{-1} from 3.0 to 6.0 V (vs. Li/Li^+), where stainless steel (SS) disks were used as the working electrodes and Li metal foils as the counter/reference electrodes.. CV test was used to study the compatibility of the electrolyte with the electrode in the voltage range of –0.5 to 6 V and at a sweep rate of 1 mV s^{-1}.

The Li^+ transference number (t_{Li}^+) of the electrolyte was obtained by the Li||Li cell via EIS and DC potentiostatic polarization measurements, and t_{Li}^+ was calculated using the Bruce-Vincent-Evans equation [3, 4]:

$$t_{Li}^+ = \frac{I_\infty(\Delta V - I_0 R_0)}{I_0(\Delta V - I_\infty R_\infty)} \quad \text{(S5)}$$

where ΔV is the applied DC polarization voltage (0.01 V) across the cell, R_0 and R_∞ represent the interfacial resistances before and after polarization, respectively; I_0 and I_∞ are the initial current before the DC polarization and the stable current after the DC polarization, respectively. Galvanostatic cycling of the Li||Li symmetric cell was conducted at room temperature with a current density of 0.5 mA cm^{-2}. Both the charge and discharge time were 0.5 h.

5. Computational methods. The Vienna Ab initio Simulation Package (VASP) with projector augmented wave (PAW) potentials was used to realize the DFT simulation.[5] During simulation process, the generalized gradient approximation (GGA) in the form of Perdew-Burke-Ernzerhof (PBE) was selected to describe the exchange and correlation effects [6, 7]. The plane wave cutoff energies of all models were fixed at 500 eV, and the convergence criteria of energy and force were set to 10^{-5} eV and 0.05 eV/Å, respectively. The Methfessel-Paxton smearing method with a sigma value of 0.2 eV was employed to smooth the electrons near the Fermi level. In addition, the number of

k-points had been rigorously tested to ensure the calculation accuracy, and spin polarization was also taken into account. The Monkhorst-Pack[8] mesh *k*-points of 7 × 5 × 5 and 9 × 9 × 7 were used for the geometric optimization of the bulk models of γ-Al_2O_3 and α-$LiAlO_2$, and 3 × 3 × 1 was employed to optimize all the slab models.

γ-Al_2O_3 and α-$LiAlO_2$ were fully relaxed before constructing the surface models. γ-Al_2O_3 belongs to $P_{21/m}$ space group and the lattice parameters were adjusted to a = 5.580 Å, b = 8.404 Å, and c = 8.072 Å. α-$LiAlO_2$ is classified to $R\bar{3}m$ space group and the lattice parameters were relaxed to $a = b$ = 2.825 Å and c = 14.342 Å. After the bulk models were fully optimized, the α-$LiAlO_2$ (101) surface[9] slab model with three layers of atoms and the γ-Al_2O_3 (111) surface[10] slab model with eight layers of atoms were selected according to the TEM observation. α-$LiAlO_2$ and γ-Al_2O_3 were combined together by expansion cell and lattice matching, and an interface model with a lattice mismatch rate of 14% was obtained to study the properties of the combination [11]. All the slab models adopted a periodic three-dimensional structure, and a vacuum layer of 15 Å was set in the *Z*-axis direction of the surface model to isolate interactions between the periodic images. After the slab model was fully relaxed, $P^{F\bar{}}_{6}$ and $Cl^{O\bar{}}_{4}$ were placed 3 Å away from the surface. The total energy of the anion-adsorbed configuration was obtained after fully relaxing the systems again. The energy of the anions was calculated by placing the anions in a periodic box with a size of 30 × 30 × 30 (Å), with the calculation parameters the same as those used in the slab models[12, 13].

The adsorption energy for the anions, E_{ad}, was calculated by:

$$E_{ad} = E_{base+anion} - \left(E_{base} + E_{anion} \right) \quad \text{(S6)}$$

where $E_{base\ +\ anion}$, E_{base}, and E_{anion} are the total energy of the anion-adsorbed system,

energy of the substrate, and energy of the anion, respectively.

6. Battery assembly and test. $LiFePO_4$ (LFP) and $LiNi_{0.85}Co_{0.05}Al_{0.1}O_2$ (NCA) cathode active materials were purchased from Shenzhen Kejing Materials Technology Co., Ltd. In a typical cathode preparing process, dehydrated commercial cathode active material (LFP or NCA), Super P, and PVDF-HFP at a weight ratio of 8:1:1 were mixed with a moderate amount of NMP and stirred for 12 h to form a homogeneous slurry, and then the cathode was made by the doctor blading method. The as-obtained cathode was dried in vacuum at 60 ℃ for 24 h. The dried LFP and NCM electrodes were controlled with areal loadings of 2-2.5 mg cm^{-2} and 3.5-4 mg cm^{-2}, respectively. Then Li-metal batteries were assembled in argon filled glovebox (Mikrouna, O_2 and H_2O content < 0.1 ppm) using fresh and smooth Li foil (Φ = 15 mm, thickness of 250 μm) as anode and the 5% LAO-PVDF electrolyte as separator in a CR2032 coin-type cell. Galvanostatic charge and discharge performances of the batteries were investigated using a LANHE CT2001A charge/discharge system (Wuhan LAND Electronics Co., Ltd.), in which LFP||Li and NCA|Li batteries were tested at room temperature in the potential range of 4.2 to 2.8 V and 4.3 to 2.6 V, respectively.

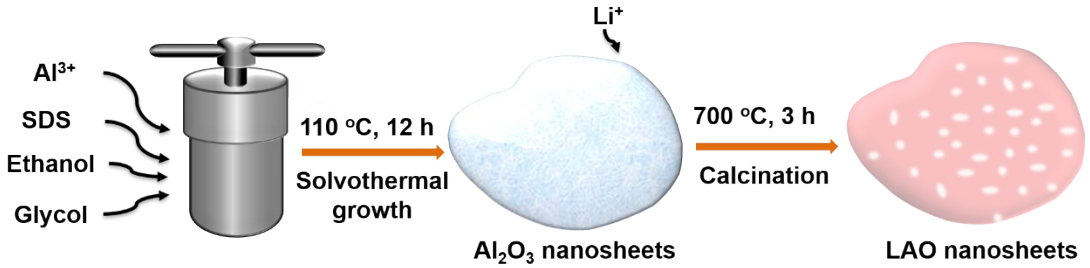

Figure S1. Synthesis process of LAO nanosheets. LAO nanosheets were synthesized by a simple solvent-thermal process and subsequent annealing treatment. At the first step, a simple solvothermal method was carried out at 110 °C for 12 h, in which aluminium isopropoxide was selected as the Al^{3+} source and sodium dodecyl sulfate (SDS) as the surfactant together with ethylene glycol co-surfactant in the ethanol solvent. At the second step, the as-prepared products were mixed with Li_2CO_3 then transformed into muffle furnace and annealed at 700 °C for 3 h.

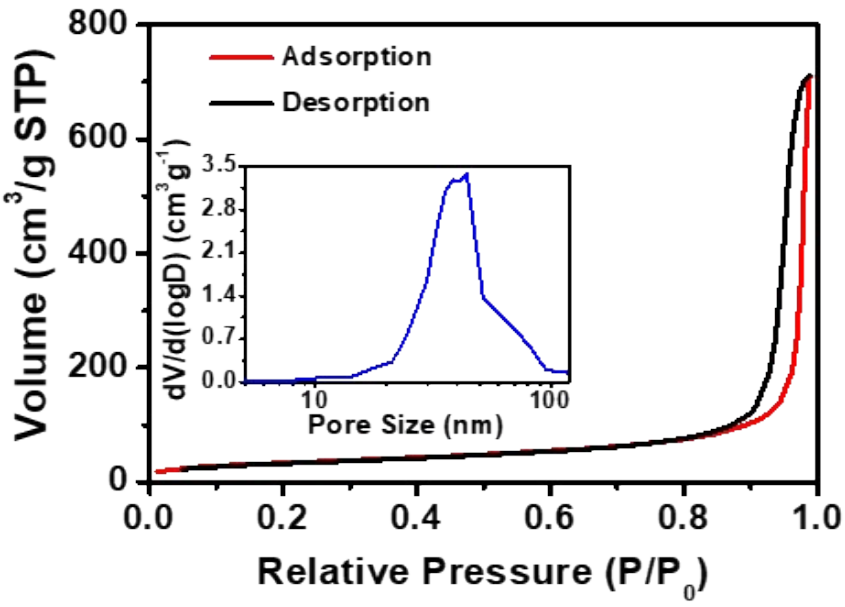

Figure S2. Nitrogen adsorption/desorption isotherms of LAO nanosheets, the inset shows the BJH pore size distribution.

The structure of the obtained LAO nanosheets was analyzed by nitrogen adsorption. The isotherms of LAO show a type-IV adsorption-desorption isotherm with a type-I hysteresis loop, indicating the existence of mesoporous structure. The prepared LAO nanosheets exhibits a Brunauer-Emmett-Teller (BET) specific surface area of 121 m^2/g. The Barrett-Joyner-Halenda (BJH) pore size distribution curve calculated from the adsorption branch, depicted as the inset, shows that the obtained LAO nanosheets have a narrowly distributed pore size centered at ~32 nm.

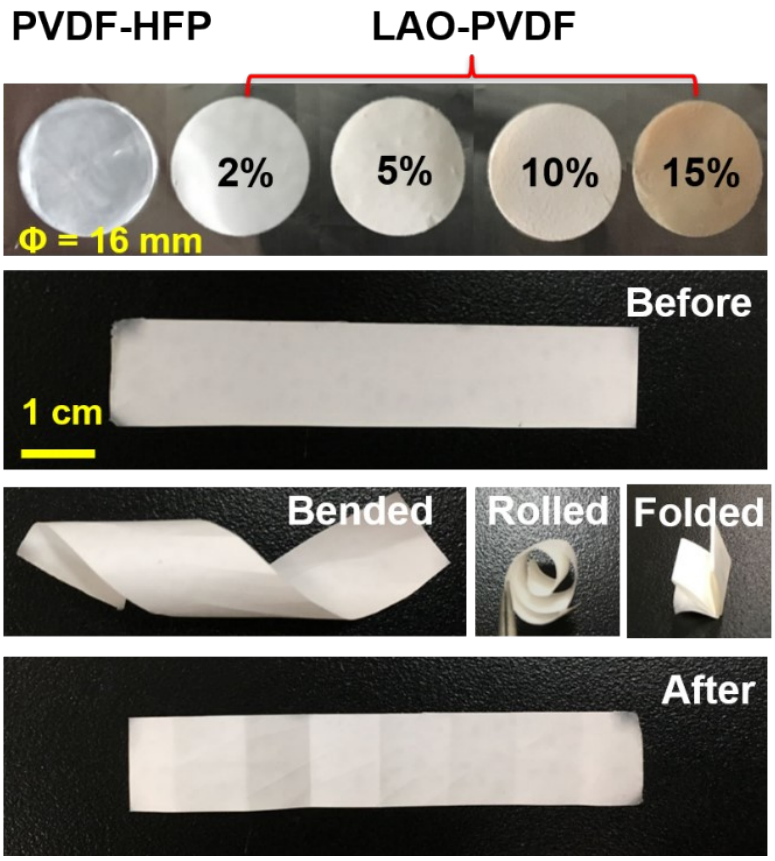

Figure S3. Photographs showing the PVDF-HFP and *x*% LAO-PVDF (*x* = 2, 5, 10, 15) membranes, and flexible LAO-PVDF membrane before and after bending, rolling, and folding.

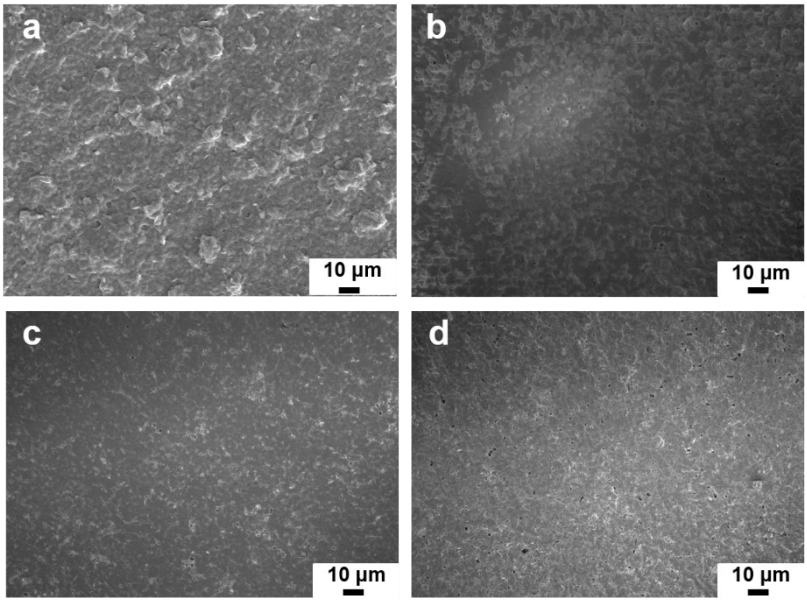

Figure S4. SEM images of the as-prepared LAO-PVDF membranes: a) PVDF-HFP, b) 2% LAO-PVDF, c) 10% LAO-PVDF, and d) 15% LAO-PVDF. All the prepared membranes have uniform, smooth, and clear surfaces.

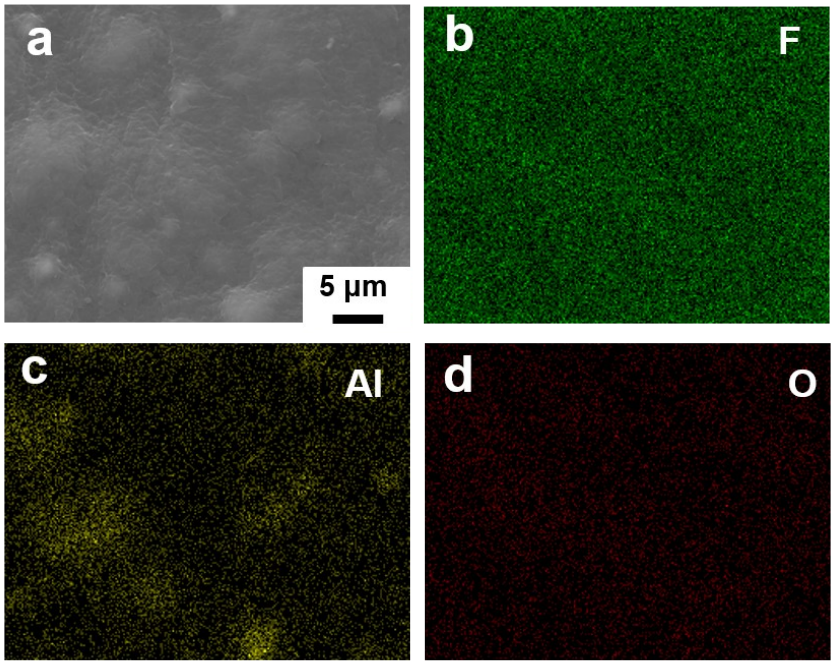

Figure S5. SEM image and elemental mapping of the 5% LAO-PVDF membrane surface. Smooth and clear surfaces can be observed, and the LAO nanosheets are homogeneously dispersed in the PVDF-HFP matrix.

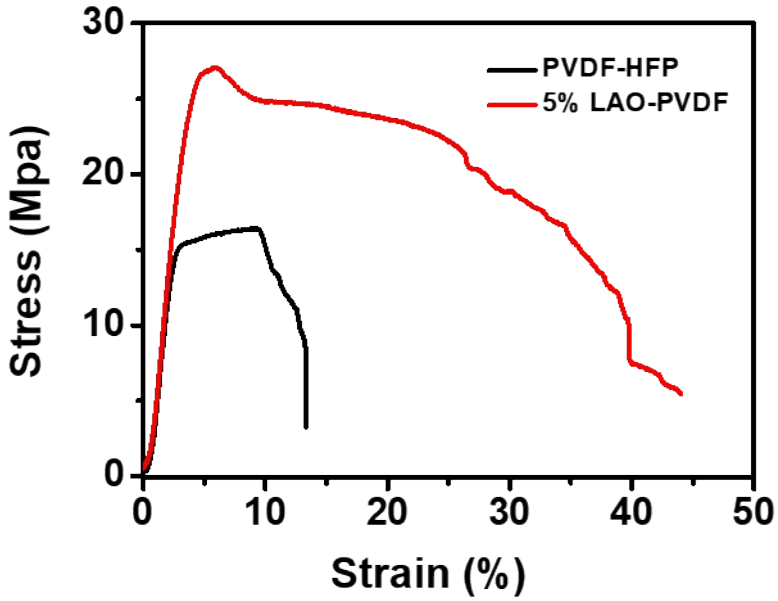

Figure S6. Stress-strain curves of the PVDF-HFP and 5% LAO-PVDF. The tensile strength of the PVDF-HFP membrane increases with LAO addition. The tensile strengths of neat PVDF-HFP and the 5% LAO-PVDF membrane are 16.4 and 27.1 MPa, respectively.

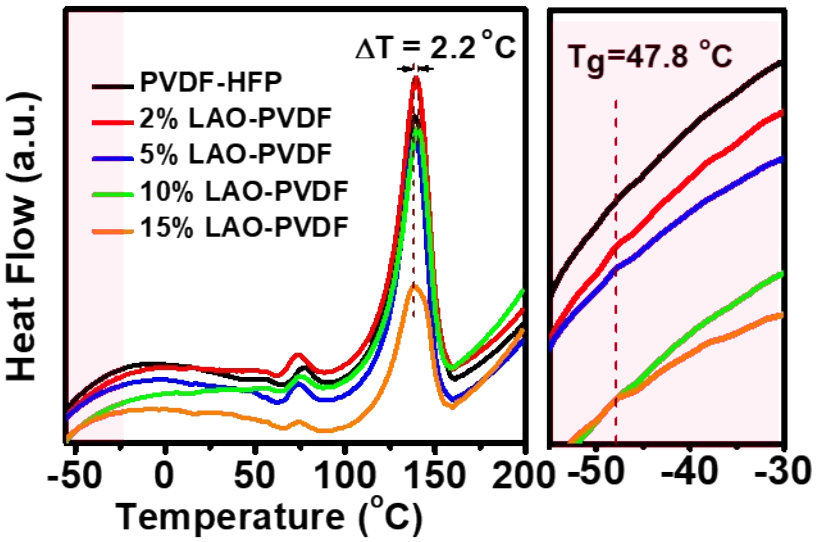

Figure S7. DSC curves of the PVDF-HFP and *x*% LAO-PVDF (*x* = 2, 5, 10, 15) membranes. The melting peak increases with LAO addition, shifts from 138.7 °C for the PVDF-HFP membrane to 140.1 °C for the LAO-PVDF membranes. The glass transition temperature of all the membrane are ~47.8 °C.

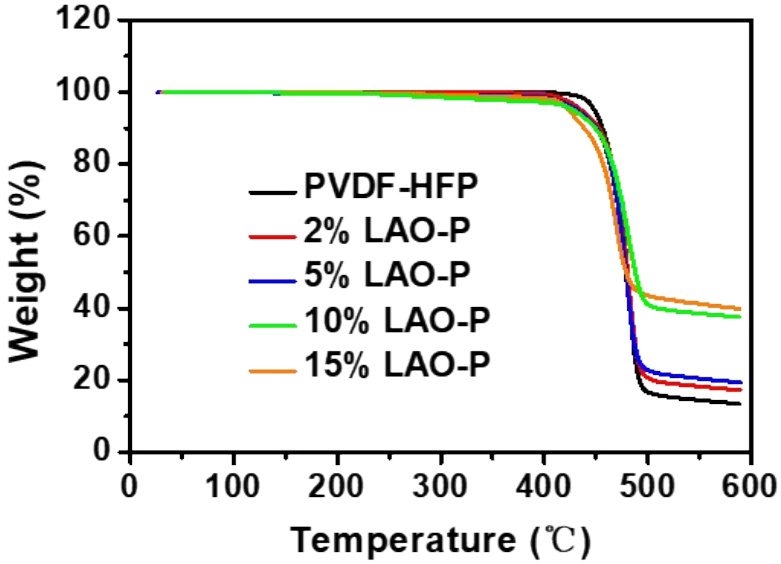

Figure S8. TGA curves of the PVDF-HFP and *x*% LAO-PVDF (*x* = 2, 5, 10, 15) membranes.

The thermal degradation temperature of PVDF-HFP is about 500 °C. With the addition of the LAO nanosheets, the thermal stability of the polymer slightly decreases. The weight loss of the membranes starts at ~300 °C, corresponding to the polymer melting and gradual degradation, which may be due to the increased amorphous fraction in the polymer electrolytes resulting from the interaction between the LAO nanosheets and the PVDF-HFP matrix.

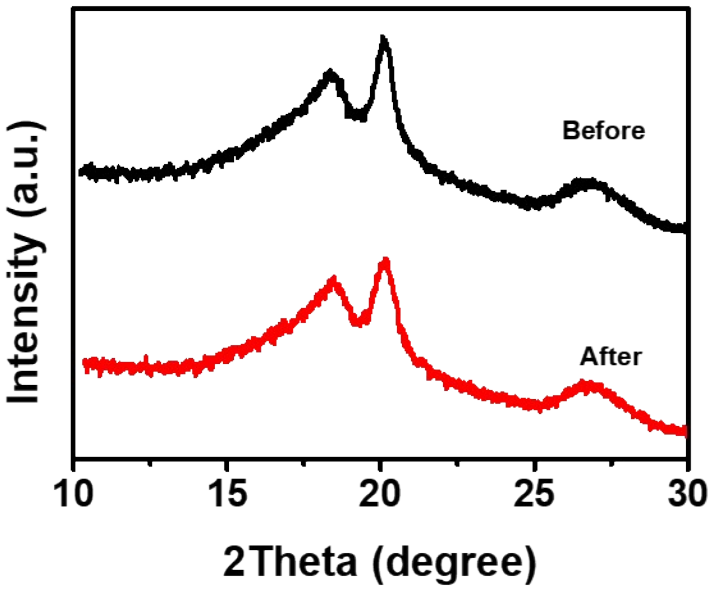

Figure S9. XRD pattern of the 5% LAO-PVDF membrane before and after immersing into LE.

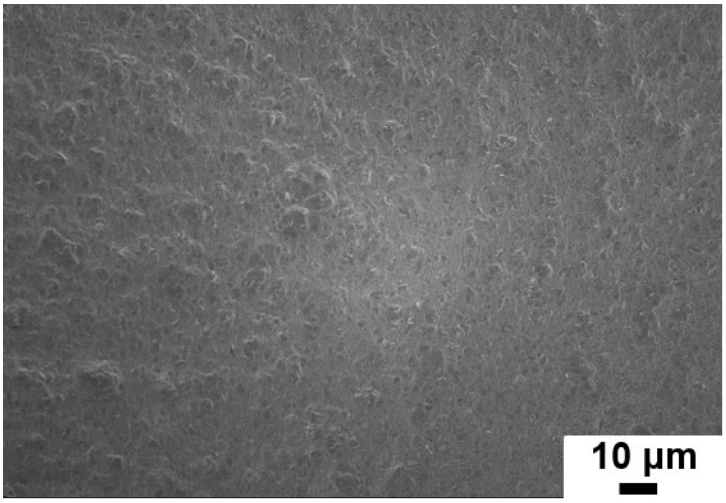

Figure S10. SEM image of the 5% LAO-PVDF electrolyte.

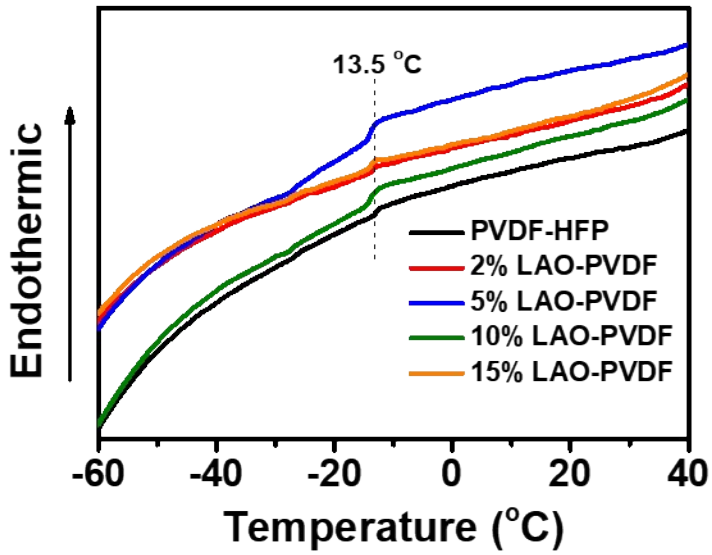

Figure S11. DSC curves of the PVDF-HFP and *x*% LAO-PVDF (*x* = 2, 5, 10, 15) electrolytes. The glass transition temperature of all the electrolytes are 13.5 °C.

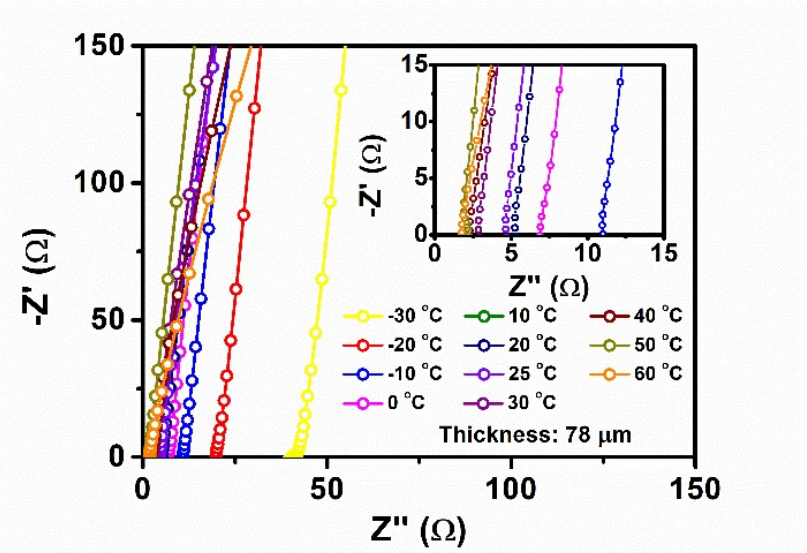

Figure S12. EIS spectra of the 5% LAO-PVDF electrolyte in the temperature range of –30 to 60 °C.

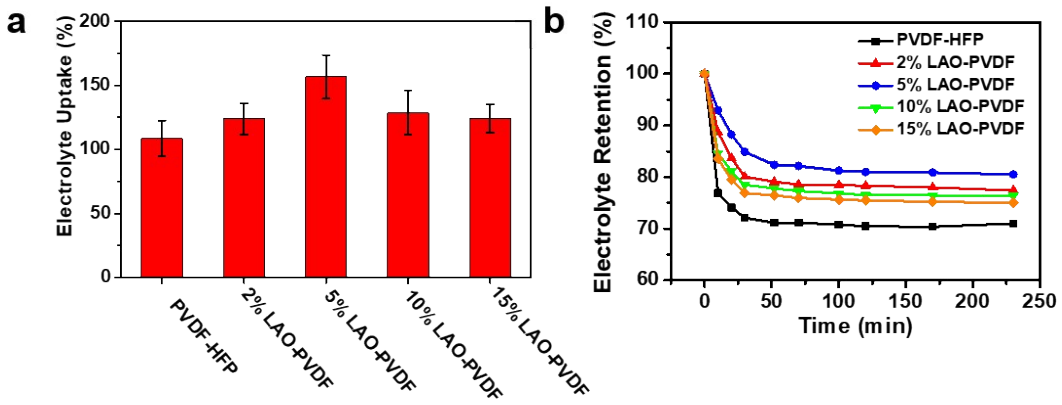

Figure S13. a) Electrolyte uptake, b) electrolyte retention of the PVDF-HFP and *x*% LAO-PVDF (*x* = 2, 5, 10, 15) electrolytes. The electrolyte uptakes of the PVDF-HFP and 2, 5, 10, 15% LAO-PVDF electrolytes are 109%, 124%, 157%, 129%, and 124%, respectively. The electrolyte retentions of the PVDF-HFP and 2, 5, 10, 15% LAO-PVDF electrolytes are 71%, 80%, 77%, 76%, and 75%, respectively.

Table S1. VTF fitting parameters of the PVDF-HFP and *x*% LAO-PVDF (*x* = 2, 5, 10, 15) electrolytes in **Figure 2a**.

Sample	A (S cm^{-1} K$^{1/2}$)	E_a (eV)	T_0 (K)
PVDF-HFP	2.113	7.9×10^{-2}	175.5
2% LAO-PVDF	0.524	4.2×10^{-2}	175
5% LAO-PVDF	0.461	3.5×10^{-2}	176
10% LAO-PVDF	0.423	4.4×10^{-2}	174
15% LAO-PVDF	0.405	4.8×10^{-2}	167

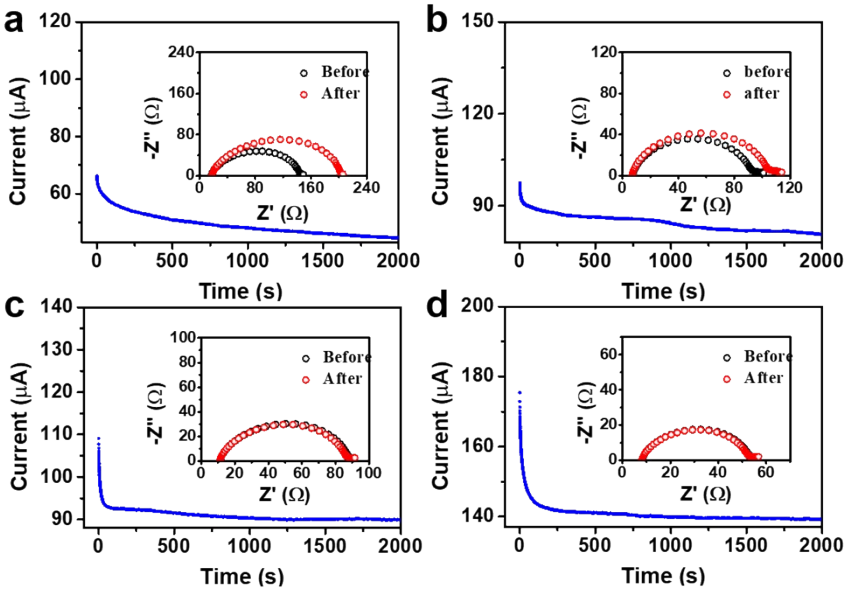

Figure S14. Measurements of t_{Li}^{+} of a) PVDF-HFP, b) 2% LAO-PVDF, c) 10% LAO-PVDF, and d) 15% LAO-PVDF electrolytes. The lithium-ion transference numbers of the PVDF-HFP and 2, 10, 15% LAO-PVDF electrolytes are 0.5, 0.69, 0.54, and 0.50, respectively.

Table S2. Measured values for the parameters in the Bruce-Vincent-Evans equation and the calculated Li^+ transference number (t_{Li}^{+}) of the PVDF-HFP and *x*% LAO-PVDF (*x* = 2, 5, 10, 15) composite electrolytes at room temperature.

Sample	I_0	I_s	R_0	R_s	$\triangle V$	t_{Li}^{+}
PVDF-HFP	65	42	128	187	0.01	0.50
2% LAO-PVDF	97.3	80.7	85	98	0.01	0.69
5% LAO-PVDF	74.7	71.0	90	96	0.01	0.92
10% LAO-PVDF	109	90	75	80	0.01	0.54
15% LAO-PVDF	175	140	45	47	0.01	0.50

Table S3. Ionic conductivities and t_{Li}^{+} at room temperature of this work as compared with published results.

	Materials	σ (mS cm^{-1})	t_{Li}^{+}	Ref.
Composite polymer electrolytes	(γ-Al_2O_3@α-$LiAlO_2$ + PVDF-HFP) + ($LiPF_6$ + EC/DMC/EMC + 1%VC)	0.85	0.92	This work
	(γ-Al_2O_3@α-$LiAlO_2$ + PVDF-HFP) + (LiTFSI + DOL/DME)	--	0.86	
	(γ-Al_2O_3@α-$LiAlO_2$ + PVDF-HFP) + ($LiClO_4$ + PC)	--	0.62	
	(PVA + Uio-66 MOF) + ($LiClO_4$ + PC)	1.5	0.79	14
	PVDF-HFP + (es-PVPSI + EC/DMC)	0.68	0.85	4
	(PVDF-HFP-La_2O_3//PVDF-HFP-BN) + ($LiPF_6$ + DEC/EMC/DMC/EC)	0.75	0.72	15
	Silane-Al_2O_3 + ($LiPF_6$ + EC/DMC)	9.98	0.84	16
	Silane-Al_2O_3 + (LiTFSI + PC)	3.89	0.88	
	Cu-MOF-74 + ($LiClO_4$ + PC)	--	0.82	17
	LiTFSI + PAN/PVEC//PEGDMA-SiO_2-Pyr_{14}TSFI	0.156	0.602	18
	PVDF@PE + ($LiPF_6$ + EC/DMC/DEC)	0.30	0.28	19
	PVDF/ZSM-Si(Al)@PE + ($LiPF_6$ + EC/DMC/DEC)	0.44	0.54	
	LiPF6+EC/DMC	0.53	0.35	20
	Uio-66 MOF + PEO + LiTFSI	0.13	0.35	21
	LLZO + PEO + LiTFSI	0.12	0.33	22
	PYR13TFSI + EMITFSI + LiTFSI	4.92	0.3	23
	LiTFSI-BEPyTFSI	1.8	0.4	24
	PVP/PVDF-HFP + ($LiBF_4$ + EC/DMC)	0.4	0.2	25
	P($EC_{0.30}$/$EO_{0.70}$) + LiTFSI	0.037	0.66	26
	Poly(PEGM)-b-poly(LiMTFSI) Copolymers	0.0023	0.83	27
Ceramic electrolytes	$Li_{3.94}Cr_{0.02}SiO_4$	0.025	0.95	28
	LLTO	0.0017	1	29
	$Li_{5.25}La_3Ta_{1.75}Ge_{0.25}O_{12}$	0.08	1	30
	1 M LiFSI/DOL/DME	--	0.314	31
	1 M LiFSI/DEE	--	0.512	32
	1 M LiFSI/DME	21.9	0.39	33
	1 M LiFSI/DMB	3.8	0.45	
	1 M LiFSI/FDMB	3.5	0.48	
	1 M LiTFSI/G2E/MFE/FEC	3.8	0.568	
	1 M LiTFSI/DME/DOL	--	0.4	34

Liquid electrolytes	7 M LiTFSI/DME/DOL	--	0.73	35
	1 M LiTFSI/DOL/DHCE	2.3	0.48	
	1 M LiTFSI/DOL/MDHCE	1.78	0.46	
	PE separator + 1 M $LiPF_6$/EC/DMC (3:7, w/w)	0.35	0.37	36
	0.1 M LiDFP + 0.4 M LiBOB in EC/DMC (3:7, w/w)	0.16	0.49	
	0.1 M LiDFP + 0.4 M LiFSI in EC/DMC (3:7, w/w)	0.26	0.58	37
	0.1 M LiDFP + 0.4 M LiTFSI in EC/DMC (3:7, w/w)	0.27	0.50	
	2.0 M LiPF6–mixTHF	5.4	0.74	

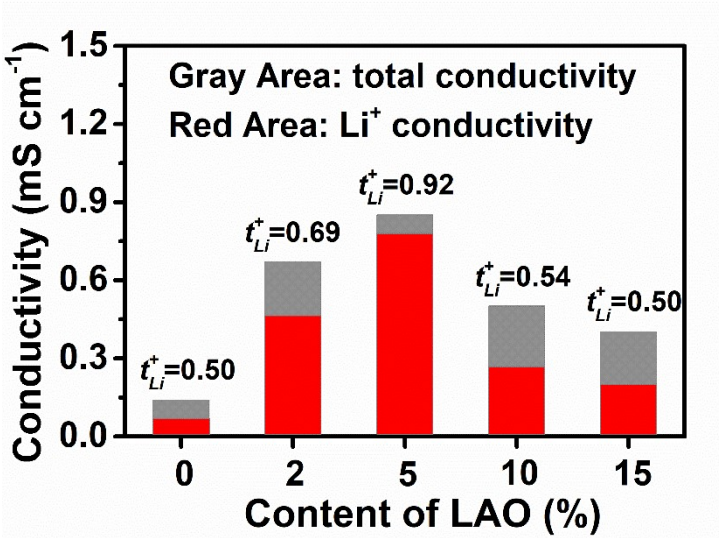

Figure S15. Comparisons of t_{Li}^{+} and ionic conductivities. The Li^+ conductivities of the PVDF-HFP and 2, 5, 10, 15% LAO-PVDF electrolytes are 0.07, 0.46, 0.78, 0.27, and 0.20 mS cm^{-1}, respectively.

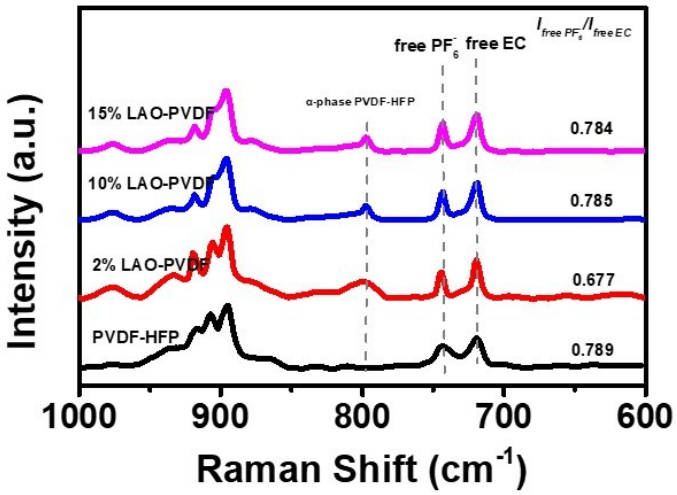

Figure S16. Raman spectra of the LAO-PVDF (x = 0, 2, 10, 15) electrolytes.

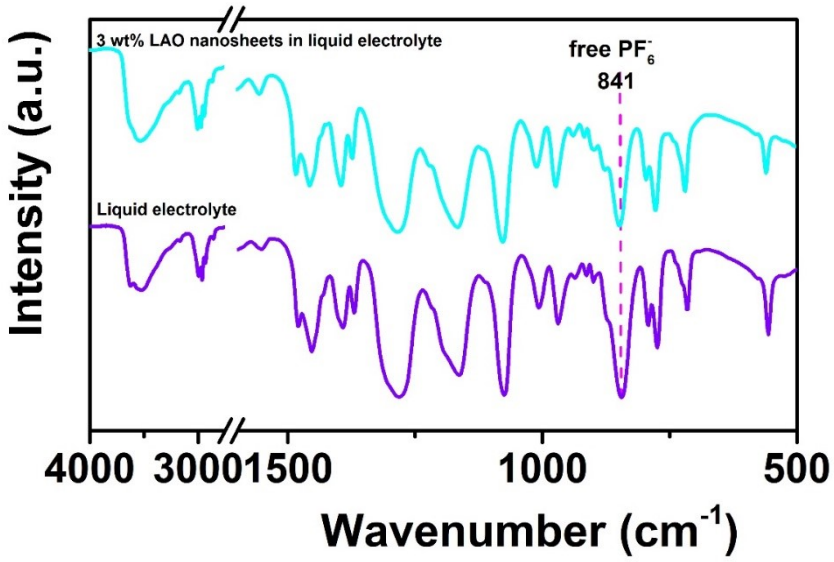

Figure S17. FTIR spectra of LE without and with 3 wt.% LAO nanosheets.

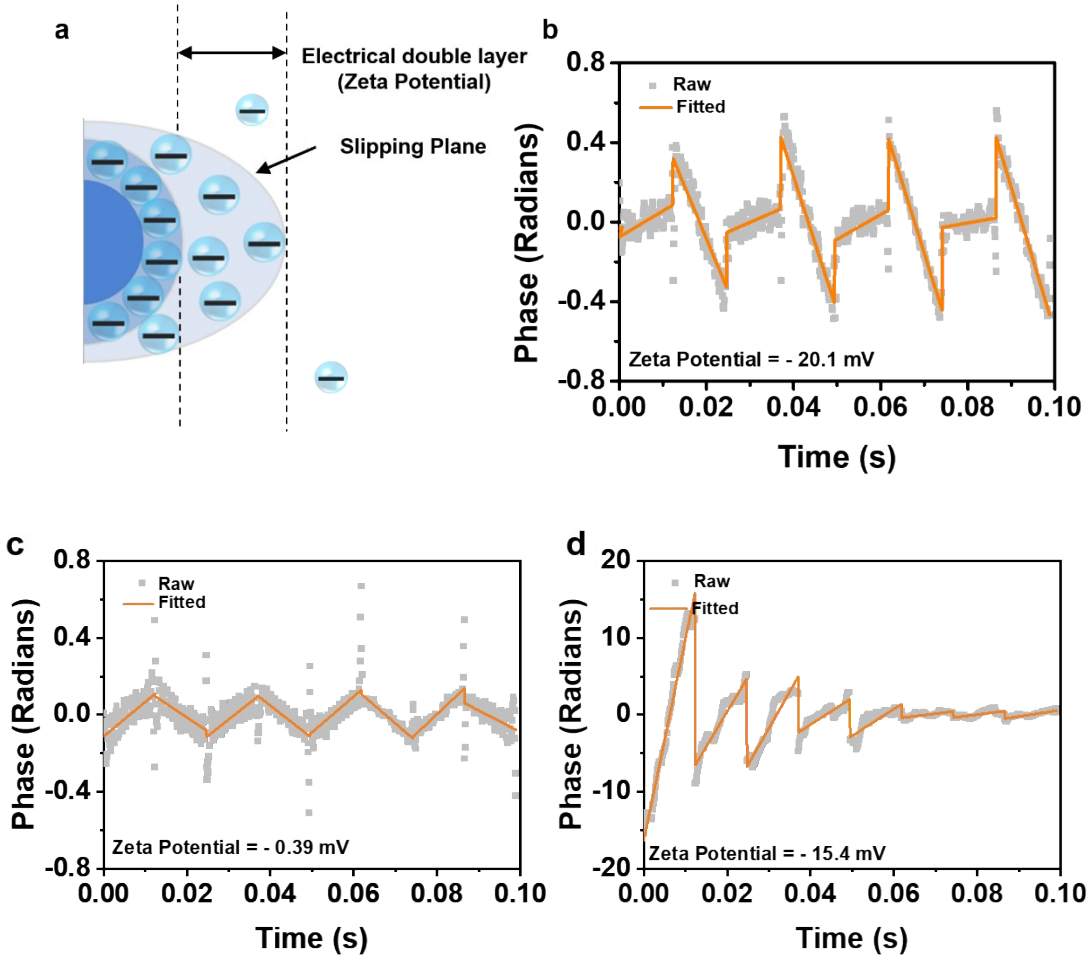

Figure S18. a) Schematic diagram of zeta-potential of the LAO nanosheets with positive surface charge. The light-blue sphere represents the attracted anions. Measured zeta potentials of b) LAO, c) γ-Al_2O_3, and d) α-$LiAlO_2$ dispersed in dimethyl carbonate (DME) solvent with 20 mM $LiPF_6$. Zeta Potential analysis is a technique for determining the surface charge of nanoparticles in solution. Nanoparticles have a surface charge that attracts a thin layer of ions of opposite charge to the nanoparticle surface.

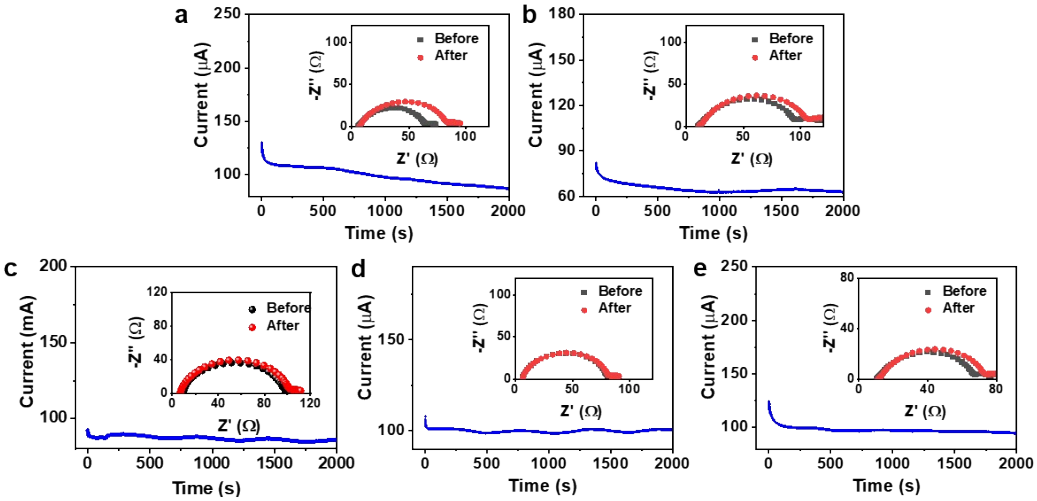

Figure S19. Time evolution of current during polarization under a voltage of 10 mV of Li||Li cells with the LAO-PVDF electrolytes with (a) 0 wt.%, (b) 20 wt.%, (c) 50 wt.%, and (d) 70 wt.% LAO, and the (e)100 wt.% α-$LiAlO_2$ electrolyte. The corresponding impedance spectra before and after polarization are shown in the inset.

Table S4. Measured values for the parameters in the Bruce-Vincent-Evans equation and the calculated Li^+ transference number (t_{Li}^+) of the PVDF-based electrolyte using LAO fillers with *x* wt.% α-$LiAlO_2$ (*x* = 0, 20, 50, 70, 100).

α-$LiAlO_2$ in LAO (%)	R_o	R_s	I_o	I_s	ΔV	t_{Li}^+
0	59	79	130.2	87.6	0.01	0.50
19	87	96	82.1	64.6	0.01	0.59
52	90	96	74.7	71	0.01	0.92
70	75	76	107.8	99	0.01	0.71
100	56	65	124.3	96.5	0.01	0.63

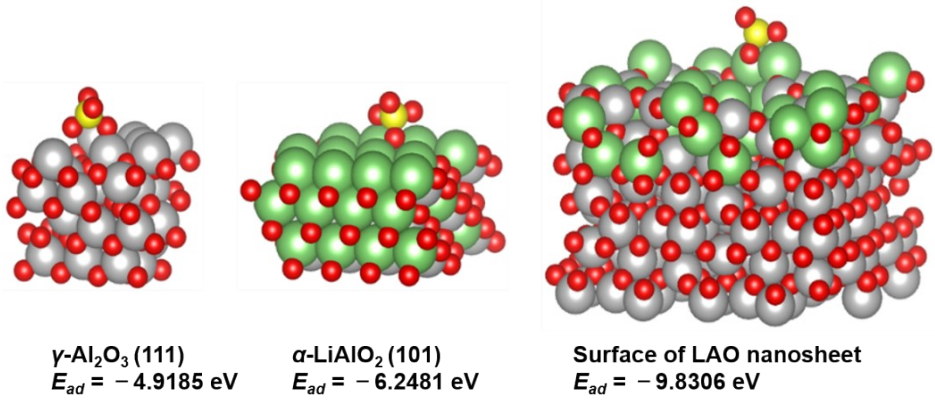

Figure S20. Configurations for DFT calculations of ClO_4^- adsorption energies on γ-Al_2O_3 (111) surface, α-$LiAlO_2$ (101) surface, and the surface of LAO nanosheet. The corresponding adsorption energies are listed at the bottom. (yellow: chlorinum; gray: aluminum; red: oxygen; green: lithium).

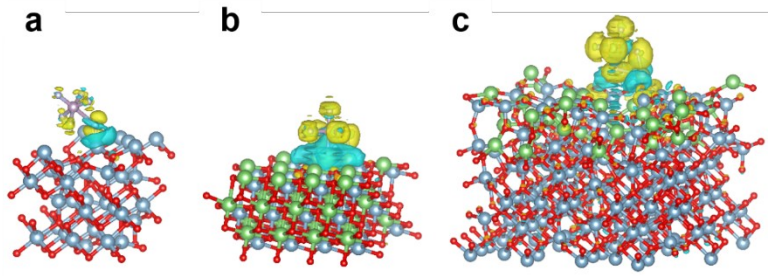

Figure S21. Differential charge density diagrams of PF_6^- adsorbed on (a) γ-Al_2O_3 (111) surface, (b) α-$LiAlO_2$ (101) surface, and (c) LAO surface.

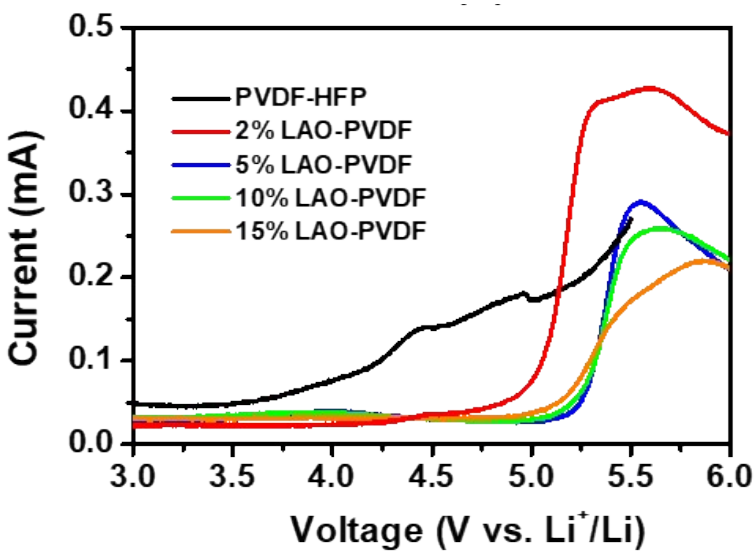

Figure S22. Linear sweep voltammetry of PVDF-HFP and *x*% LAO-PVDF (*x* = 2, 5, 10, 15) electrolytes at room temperature over the potential range from 3.0 to 6.0 V at a sweep rate of 10 mV s^{-1}. The electrochemical windows of 5%, 10%, and 15% LAO-PVDF are found to be >5.2 V *vs.* Li^+/Li at room temperature, which is higher than that of 2% LAO-PVDF (~4.3 V *vs.* Li^+/Li) and PVDF-HFP (~3.7 V *vs.* Li^+/Li) electrolytes.

Figure S23. Cyclic voltammetry curves of SS|5% LAO-PVDF|Li cells under a sweep rate of 1 mV s^{-1}.

The electrochemical stability and Li^+ stripping/plating kinetics of electrolytes were evaluated by cyclic voltammetry (CV) tests with a two-electrode system at 1 mV s^{-1}. The two predominant redox peaks at −0.5 to 1.0 V (*vs.* Li^+/Li) are attributed to the Li^+ plating and stripping processes on the working electrode. The enlarged CV curves from 5.0 to 6.0 V are shown in the inset, displaying that the 5% LAO-PVDF electrolyte is chemically stable up to 5.2 V, which is consistent with the LSV results in **Figure S22**.

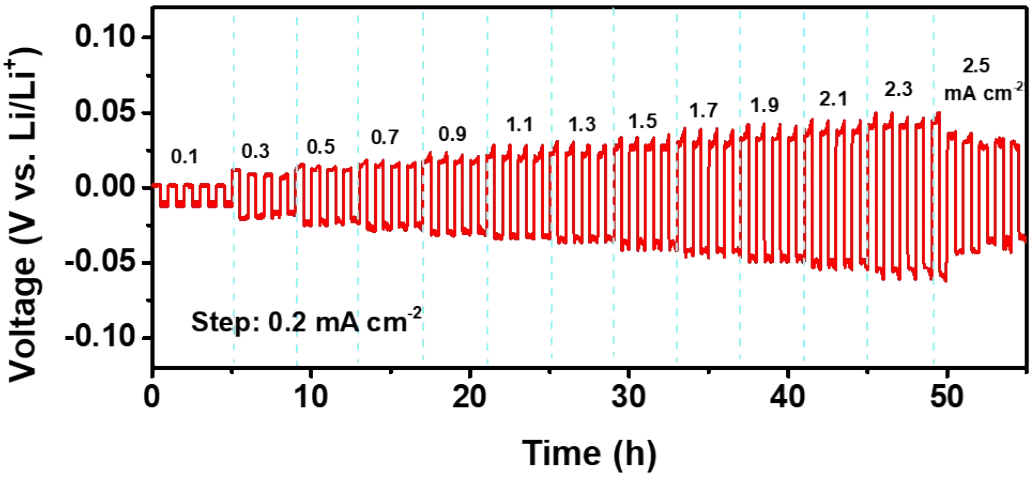

Figure S24. Voltage-time profiles of the 5% LAO-PVDF electrolyte under step-increasing current densities with the testing scheme of 30 min plating/stripping per cycle and 4 charge/discharge cycles per current density at room temperature.

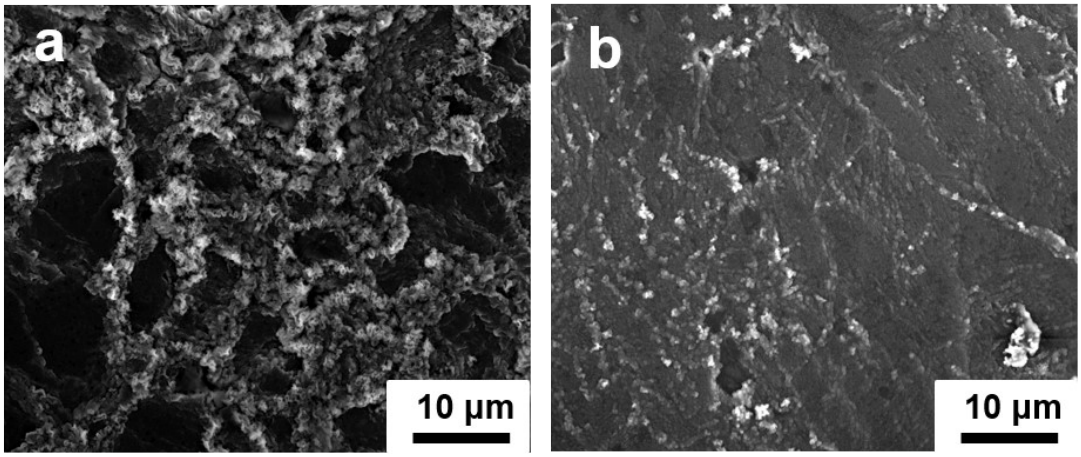

Figure S25. SEM images of the Li electrodes of (a) Li|LE|Li and (b) Li|5% LAO-PVDF|Li cells after Li stripping/plating cycling test.

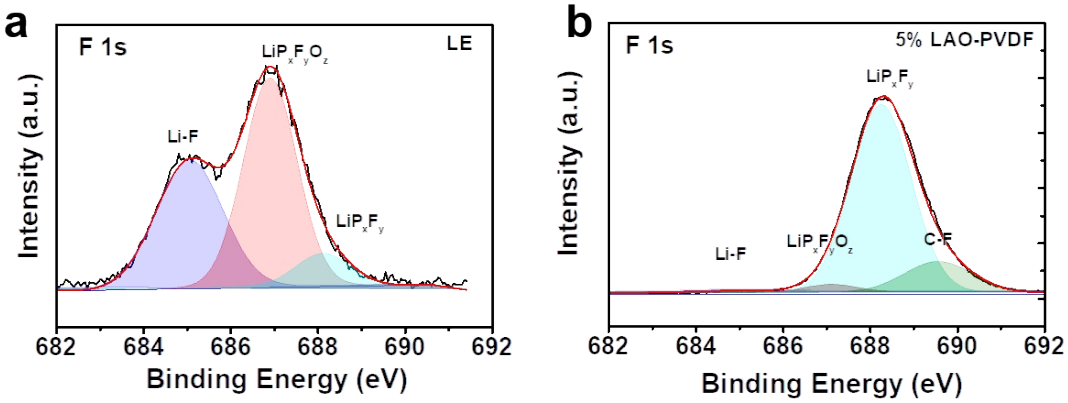

Figure S26. XPS spectra of F 1s, and the corresponding fitting peaks of the cycled Li electrodes of (a) Li|LE|Li and (b) Li|5% LAO-PVDF|Li cells after Li stripping/plating cycling test.

F 1s peaks were detected on the surfaces of the metallic Li anodes. The binding energies in the XPS spectra were referencing C 1s at 284.6 eV. The F1s spectrum was fitted with three peaks: Li-F at 685.5 eV, $LiP_xF_yO_z$ at 686.9 eV, $LiPF_6$ at 688.6 eV, and C-F bond at 689 eV. The Li|5% LAO-PVDF|Li cell has a higher ratio of $LiPF_6$ than that of Li|LE|Li cell, indicating that less PF_6^- anions are decomposed in the 5% LAO-PVDF electrolyte, because the anion-absorbing ability of LAO protects $LiPF_6$ from reacting with the Li anode.

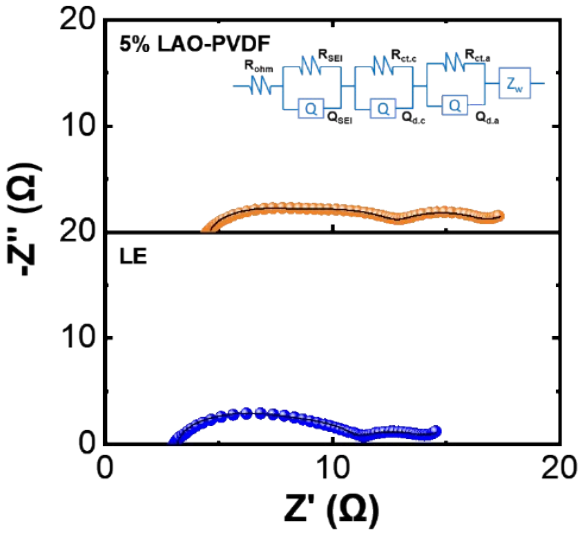

Figure S27. Nyquist plots measured when the batteries were charged to 3.9 V. The equivalent circuit for fitting of impedance data is shown in the inset.

Table S5. The fitting results of EIS spectra of NCA|LE|Li and NCA|5% LAO-PVDF|Li batteries using the equivalent circuit.

	R_{ohm}	R_{SEI}	R_{ct}	
			Rct.c	Rct.a
LE	3.2	4.7	2.8	3.1
5% LAO-PVDF	4.6	3.4	4.9	3.3

Figure S27 presents the EIS spectra of the NCA|LE|Li and NCA|5% LAO-PVDF|Li batteries when charging to 3.9 V. All the spectra could be fitted to an equivalent circuit (inset in **Figure S27**) and the corresponding fitted values are listed in **Table S5**, where R_{ohm} is the ohmic resistance, R_{SEI} is the resistance related to the migration of Li^+ through the surface film, and R_{ct} is the interfacial charge transfer resistance. The fitted resistance of the NCA|5% LAO-PVDF|Li battery is larger than that of the NCA|LE|Li battery, suggesting higher η_{ohm} and η_{ct} values.

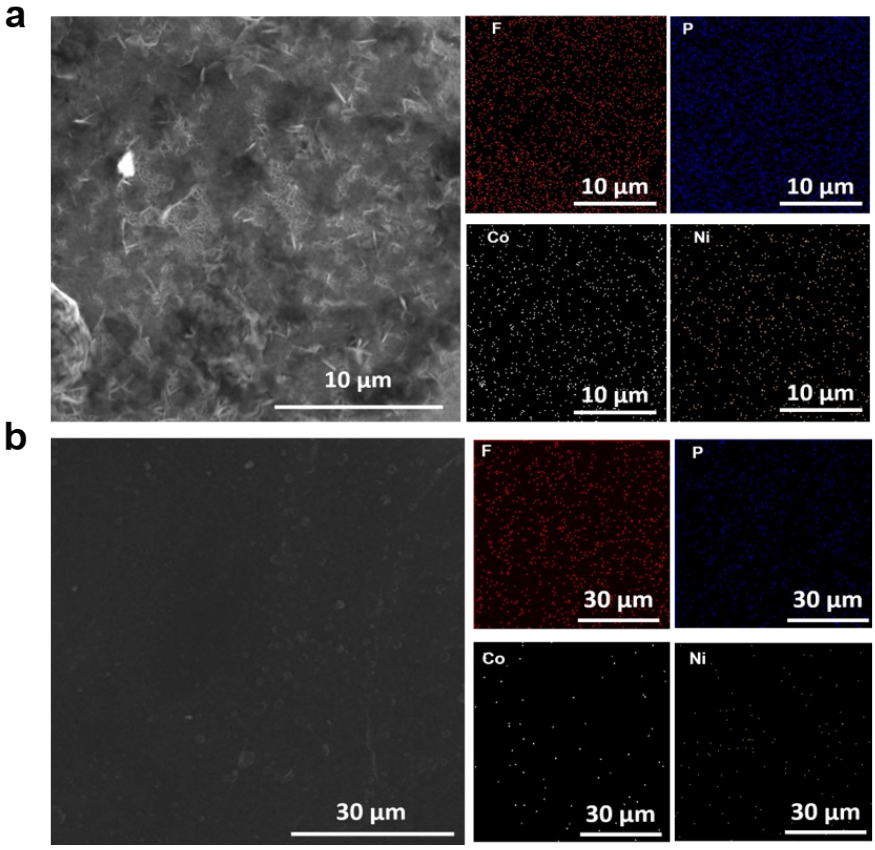

Figure S28. SEM images of the Li anodes of (a) NCA|LE|Li and (b) NCA|5%LAO-PVDF|Li after cycling, and the corresponding EDS mappings of F, P, Co, and Ni elements.

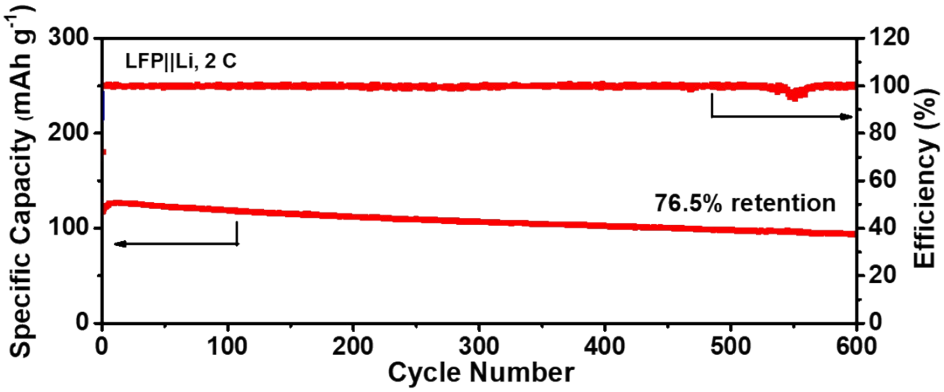

Figure S29. Cycling stability of the LFP||Li battery with PVDF-HFP electrolyte at 2C.

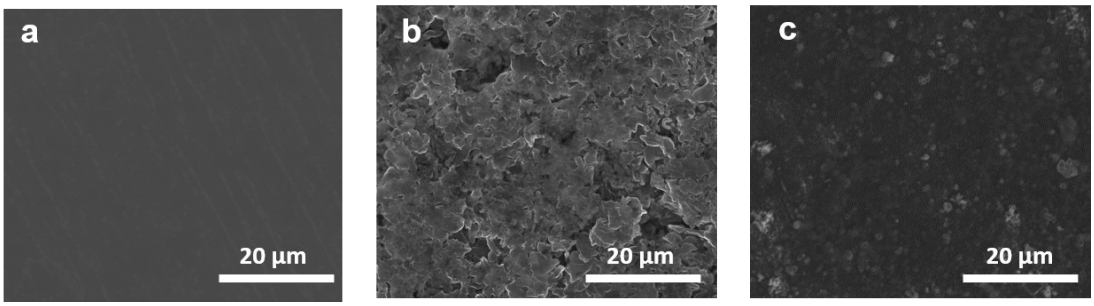

Figure S30. SEM images of (a) fresh Li plate, and the Li anodes of (b) LFP|LE|Li and (c) LFP|5%LAO-PVDF|Li batteries after cycling.

References

1. G. Chen, F. Zhang, Z. Zhou, J. Li and Y. Tang, *Adv. Energy Mater.*, 2018, **8**, 1801219.
2. D. Xie, M. Zhang, Y. Wu, L. Xiang and Y. Tang, *Adv. Funct. Mater.*, 2020, **30**, 1906770.
3. J. Evans, C. A. Vincent and P. G. Bruce, *Polymer*, 1987, **28**, 2324-2328.
4. C. Li, B. Qin, Y. Zhang, A. Varzi, S. Passerini, J. Wang, J. Dong, D. Zeng, Z. Liu and H. Cheng, *Adv. Energy Mater.*, 2019, **9**, 1803422.
5. P. E. Blochl, *Phys. Rev. B*, 1994, **50**, 17953-17979.
6. G. Kresse and J. Furthmüller, *Phys. Rev. B*, 1996, **54**, 11169-11186.
7. J. P. Perdew, K. Burke and M. Ernzerhof, *Phys. Rev. Lett.*, 1996, **77**, 3865-3868.
8. H. J. Monkhorst and J. D. Pack, *Phys. Rev. B*, 1976, **13**, 5188-5192.
9. S. J. Heo, R. Batra, R. Ramprasad and P. Singh, *J. Phys. Chem. C*, 2018, **122**, 28797-28804.
10. M. Digne, P. Sautet, P. Raybaud, P. Euzen and H. Toulhoat, *J. Catal.*, 2004, **226**,

54-68.

11. M. Yu, W. Qu, S. Xu, L. Wang, B. Liu, L. Zhang and J. Peng, *Comp. Mater. Sci.*, 2018, **153**, 217-227.

12. S. Kheirjou and A. Fattahi, *J. Phys. Org. Chem.*, 2018, **31**, e3798.

13. S. Miyoshi, T. Akbay, T. Kurihara, T. Fukuda, A. T. Staykov, S. Ida and T. Ishihara, *J. Phys. Chem. C*, 2016, **120**, 22887-22894.

14. C. Zhang, L. Shen, J. Shen, F. Liu, G. Chen, R. Tao, S. Ma, Y. Peng and Y. Lu, *Adv. Mater.*, 2019, **31**, e1808338.

15. M. Waqas, S. Ali, D. Chen, B. Boateng, Y. Han, M. Zhang, J. Han, J. B. Goodenough and W. He, *Compos. Part B-Eng.*, 2019, **177**, 107448.

16. H. Xu, Y. He, Z. Zhang, J. Shi, P. Liu, Z. Tian, K. Luo, X. Zhang, S. Liang and Z. Liu, *J. Energy Chem.*, 2020, **48**, 375-382.

17. S. Yuan, J. L. Bao, J. Wei, Y. Xia, D. G. Truhlar and Y. Wang, *Energ. Enviorn. Sci.*, 2019, **12**, 2741-2750.

18. K. Wen, X. Tan, T. Chen, S. Chen and S. Zhang, *Energy Storage Mater.*, 2020, **32**, 55-64.

19. X. Mao, L. Shi, H. Zhang, Z. Wang, J. Zhu, Z. Qiu, Y. Zhao, M. Zhang and S. Yuan, *J. Power Sources*, 2017, **342**, 816-824.

20. R. Zahn, M. F. Lagadec, M. Hess and V. Wood, *ACS Appl. Mater. Inter.*, 2016, **8**, 32637-32642.

21. J.-F. Wu and X. Guo, *J. Mater. Chem. A*, 2019, **7**, 2653-2659.

22. Z. Li, W.-X. Sha and X. Guo, *ACS Appl. Mater. Inter.*, 2019, **11**, 26920-26927.

23. Y. An, P. Zuo, X. Cheng, L. Liao and G. Yin, *Int. J. Electrochem. Sci*, 2011, **6**, 2398.

24. A. Fernicola, F. Croce, B. Scrosati, T. Watanabe and H. Ohno, *J. Power Sources*, 2007, **174**, 342-348.

25. Z. Wang and Z. Tang, *Mater. Chem. Phys.*, 2003, **82**, 16-20.

26. Y. Tominaga, K. Nakano and T. Morioka, *Electrochim. Acta*, 2019, **312**, 342-348.

27. L. Porcarelli, A. S. Shaplov, M. Salsamendi, J. R. Nair, Y. S. Vygodskii, D. Mecerreyes and C. Gerbaldi, *ACS Appl. Mater. Inter.*, 2016, **8**, 10350-10359.

28. S. B. R. S. Adnan and N. S. Mohamed, *Ceramics International*, 2014, **40**, 5033-5038.

29. Z. Hu, J. Sheng, J. Chen, G. Sheng, Y. Li, X.-Z. Fu, L. Wang, R. Sun and C.-P. Wong, *New Journal of Chemistry*, 2018, **42**, 9074-9079.

30. M. Kotobuki, S. Song, R. Takahashi, S. Yanagiya and L. Lu, *J. Power Sources*, 2017, **349**, 105-110.

31. J. Holoubek, H. Liu, Z. Wu, Y. Yin, X. Xing, G. Cai, S. Yu, H. Zhou, T. A. Pascal, Z. Chen and P. Liu, *Nat. Energy*, 2021, **6**, 303-313.

32. Z. Yu, H. Wang, X. Kong, W. Huang, Y. Tsao, D. G. Mackanic, K. Wang, X. Wang, W. Huang, S. Choudhury, Y. Zheng, C. V. Amanchukwu, S. T. Hung, Y. Ma, E. G. Lomeli, J. Qin, Y. Cui and Z. Bao, *Nat. Energy*, 2020, **5**, 526-533.

33. K. Deng, Q. Zeng, D. Wang, Z. Liu, G. Wang, Z. Qiu, Y. Zhang, M. Xiao and Y. Meng, *Energy Storage Mater.*, 2020, **32**, 425-447.

34. H. Yang, J. Li, Z. Sun, R. Fang, D.-W. Wang, K. He, H.-M. Cheng and F. Li, *Energy Storage Mater.*, 2020, **30**, 113-129.

35. Z. Jiang, Z. Zeng, W. Hu, Z. Han, S. Cheng and J. Xie, *Energy Storage Mater.*, 2021, **36**, 333-340.

36. H. Zheng, H. Xiang, F. Jiang, Y. Liu, Y. Sun, X. Liang, Y. Feng and Y. Yu, *Adv. Energy Mater.*, 2020, **10**, 2001440.

37. J. Chen, Q. Li, T. P. Pollard, X. Fan, O. Borodin and C. Wang, *Mater. Today*, 2020, **39**, 118-126.